Journal of Marine Research, 60, 121–150, 2002

Structure of the internal boundary layer over a patch of pinnid bivalves (*Atrina zelandica*) in an estuary

by Vladimir Nikora[1], Malcolm O. Green[2,3], Simon F. Thrush[2], Terry M. Hume[2] and Derek Goring[1]

ABSTRACT

Measurements of tidal-current boundary-layer flow over an experimental 2-m by 2-m patch of pinnid bivalves (*Atrina zelandica*) in a northern New Zealand estuary are presented. Previous work demonstrated a link between "mesoscale" (order 100 m) patchiness of the benthic biota and time-averaged boundary-layer dynamics. The aim in this new experiment was to describe the three-dimensional structure of turbulence at the patch scale (order 1 m). Flow over three densities of *Atrina* was investigated: 340 individuals per 4 m^2, 50 individuals per 4 m^2 and zero individuals. An internal boundary layer (IBL) grows downstream from the leading edge of the patch at the base of the ambient boundary layer. One meter in from the leading edge, the top of the IBL was ~12 cm above the bed for the high-density patch and ~6 cm for the low-density patch. Flow in the IBL was three-dimensional in that vertical and transverse mean velocities were nonzero, secondary Reynolds stresses were nonzero and comparable with the primary stress, and velocity spectra deviated from scaling relationships for two-dimensional flow. Thus, the observed IBL was still in its infancy, i.e., it consisted of a roughness sublayer only as the distance from the leading edge of the patch was not enough for development of a second, overlying logarithmic layer. In summary, the IBL that envelops the *Atrina* patch is a region of lower mean longitudinal velocities but more energetic turbulence relative to the ambient boundary layer. The former translates into shelter, which some organisms might take advantage of, and the latter translates into increased vertical exchange across the top of the IBL, which might enhance fluxes of nutrients, colonists and suspended sediments, and might have implications for deposition and resuspension of organically rich biodeposits. The results extend our knowledge of turbulence over patches of suspension feeders at the 1-m scale and therefore provide information needed to improve depiction of flow in models of suspension-feeder–flow interactions.

1. Introduction

Recent studies emphasise the importance of interactions between suspension feeders and near-bed flows (e.g., Wildish and Kristmanson, 1984, 1997; Ertman and Jumars, 1988; Frechette *et al.,* 1989; Monismith *et al.,* 1990; Cole *et al.,* 1992; O'Riordan *et al.,* 1993, 1995; Butman *et al.,* 1994; Jorgensen, 1996; Green *et al.,* 1998). Most of these studies addressed animal–flow interactions and phytoplankton depletion over suspension-feeder

1. NIWA, National Institute of Water and Atmospheric Research, P.O. Box 8602, Christchurch, New Zealand.
2. NIWA, National Institute of Water and Atmospheric Research, P.O. Box 11-115, Hamilton, New Zealand.
3. Corresponding author. ***email: m.green@niwa.cri.nz***

beds from the standpoint of "bulk" (integral or averaged) flow characteristics. A few studies also provided insight into mechanisms of interaction (e.g., Ertman and Jumars, 1988; Monismith *et al.,* 1990; O'Riordan *et al.,* 1993, 1995; Wildish and Kristmanson, 1997). The main limitation of the previous work is that turbulence properties, which must be a first-order control on suspension-feeder–flow interactions, were not measured in detail. For instance, Monismith *et al.* (1990) only measured longitudinal velocity over a single pair of siphons.

Suspension-feeder–flow interactions occur over a wide range of spatial scales, from the smallest scale of an individual organism to the scale of the landscape mosaic of suspension-feeder patches, which is often commensurate with external scales of the flow itself (e.g., estuary size). Such a wide range of scales suggests that different processes are relevant at different scales. Conceptually, we can separate processes into three groups (Table 1): (1) processes acting at the scale of the individual organism; (2) processes acting at the scale of the individual patch; and (3) processes acting at the scale of the landscape mosaic. In this paper we focus on processes at the patch scale for the case of pinnid bivalves (*Atrina zelandica*) in tidal currents in a northern New Zealand estuary. It represents further development of the previous study of Green *et al.* (1998), which was conducted at the landscape-mosaic scale. Green *et al.* (1998) related the steady-flow drag coefficient measured at 100 cm above the bed to the areal density of individual *Atrina* and found that there was a critical density of shells that induced flow skimming and a corresponding decrease in the drag coefficient. The results demonstrated a link between "mesoscale" (order 100 m) patchiness of the benthic biota and the time-averaged boundary-layer dynamics.

Our aim in this paper is to resolve the influence of *Atrina* on flow at a finer scale (order 1 m) by describing the three-dimensional structure of turbulence at the patch scale (Table 1). Turbulence properties are reported in the context of the "internal boundary layer" that is attached to the *Atrina* patch and that grows downstream from the leading edge of the patch at the expense of the "ambient boundary layer." Properties of the internal boundary layer (comprising only a roughness sublayer due to a limited development length) are compared with properties of the ambient boundary layer (comprising both a roughness sublayer and an overlying logarithmic layer) that is attached to the seabed devoid of *Atrina.*

Although strictly nonsiphonate bivalves, *Atrina* do fuse their mantel to form discrete inhalant and exhalant vents. Individuals sit with approximately one-third their body length protruding above the sediment surface. Compared to mytilids, which usually form dense patches with very little inter-individual space, individuals in patches of the pinnid bivalve *Atrina* ("horse mussel") are widely spaced. Thus, *Atrina* patches are very different in structure compared to patches of *Mytilis edulis* (blue mussel), which have been the primary focus of other bivalve–flow interaction studies (e.g., Frechette *et al.,* 1989; Butman *et al.,* 1994; Wildish and Kristmanson, 1997).

The results extend our knowledge of turbulence over patches of suspension feeders and provide information that is needed to improve the depiction of flow in models of

Table 1. Scales, processes and basic equations pertinent to suspension-feeder–flow interactions.

Scale region	Scales	Processes	Equations
Organism scale	Millimeters—centimeters	1. Form drag and vortex shedding. 2. Excurrent jet and incurrent suction. 3. Local mixing and water processing. *Domain:* benthic boundary layer.	*For fluid:* time-averaged continuity, momentum (Reynolds) and turbulent-energy equations. *For suspensions:* time-averaged mass-conservation (diffusion) equation.
Patch scale	Meters—tens of meters	1. Cooperative effects of the processes at the organism scale. 2. Development of the internal boundary layer. 3. Edge effects at patch boundaries. *Domain:* benthic boundary layer for small patches and, for large patches, the total depth (i.e., including the benthic boundary layer, the outer layer and the near-surface flow region).	*For fluid:* spatially averaged (in the plane parallel to the bed) Reynolds and turbulent-energy equations. *For suspensions:* spatially averaged (in the plane parallel to the bed) mass-conservation (diffusion) equation. *Averaging window:* much larger than the organism scale and smaller than (or equal to) patch size. The averaging window serves as both a scale separator and a process integrator.
Landscape mosaic scale	Hundreds of meters—kilometers	1. Cooperative effects of the processes at the patch scale. 2. Interactions between internal boundary layers formed over patches and over inter-patch areas. *Domain:* the total flow (over depth and in the plane).	*For fluid:* spatially averaged (in the plane and over depth) Reynolds equations. *For suspensions:* spatially-averaged (in the plane and over depth) mass-conservation (diffusion) equation. *Averaging window:* much larger than the characteristic scale of patches and smaller than (or equal to) the flow (i.e., estuary) itself. Again, the averaging window serves as both a scale separator and process integrator.

suspension-feeder–flow interactions. The results may also provide some insight into how these animals can influence the distribution of other members of the benthic community (Warwick *et al.,* 1997; Cummings *et al.,* 1998).

2. Field measurements

Field measurements were made in the Te Kapa arm of the Mahurangi Harbor, North Island, New Zealand (Fig. 1a). In the area where the experiment was carried out, the arm is ~1 km wide and 1–3 m deep at low tide. Circulation in the estuary is driven primarily by the semi-diurnal tide. Neap tide range is 1.4 m and spring range is 3.1 m. Tidal currents at 100 cm above the bed range from ~0.1 m/s on neap tides to ~0.2 m/s on springs. The bed material is a fine-grained sandy silt. Overall, the seabed, as follows from underwater

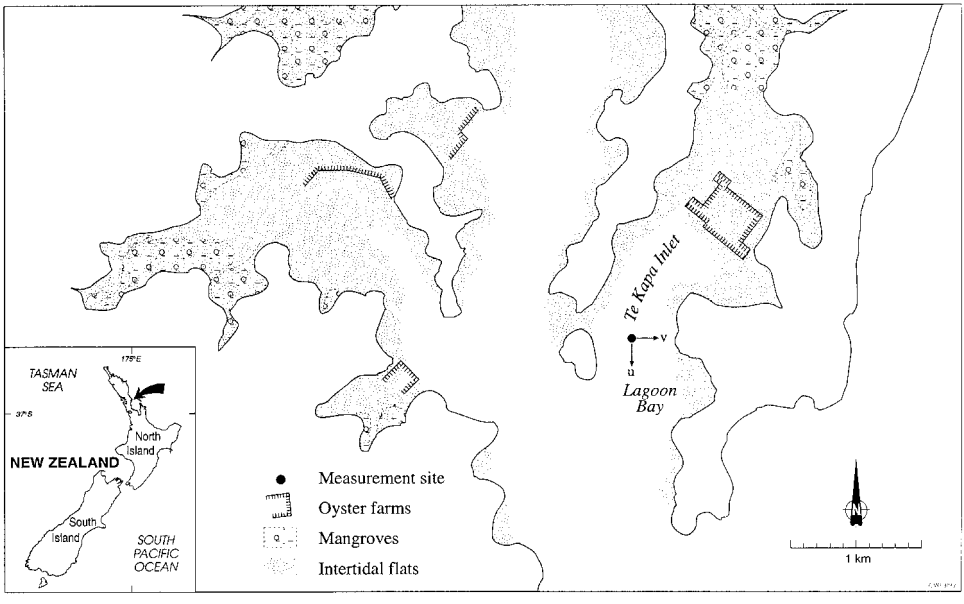

Figure 1. (a) Location map and schematics showing (b) *Atrina* density for the three sets of experiments and (c) average elevations above bed at which velocity was measured. See Figure 2 for depiction of boundary-layer structure.

pictures and visual observations, is essentially flat (i.e., no bedforms were observed) and the surface is stabilized by algal mats. Bed microtopography is characterized by crab burrows of ~1 cm diameter (approximately 60–70 burrows per m^2), bumps and hollows (probably of biological origin) ~10 cm across and 1–2 cm deep. The experimental site was the same as Site #1 in the companion paper of Green *et al.* (1998), which contains additional information.

An area of ~100 m radius devoid of *Atrina* was selected for the experiment and a 2-m by 2-m plot in that area was planted with 340 *Atrina* individuals that were harvested from a nearby site. The plot was planted 6 weeks in advance of the actual experiment to give the *Atrina* time to establish themselves and the surface sediment time to stabilize. The shells varied in width between 8–11 cm (average 8.8 cm for $N = 35$) and protruded 4–9 cm above the bed. The shells were oriented randomly, as they are in natural patches (Green *et al.,* 1998). The experimental plot size and density of individuals within the plot are similar to size and density of natural patches in the estuary (Green *et al.,* 1998).

An Acoustic Doppler Velocimeter (ADV) (Kraus *et al.,* 1994) was used to measure water velocity above and between *Atrina* in the experimental patch. The *X*-axis, which corresponds to the *u* (longitudinal) velocity component, was oriented in the positive direction seaward along the main channel. The *Y*-axis, which corresponds to the *v* (transverse) velocity component, was oriented in the positive direction toward the left bank (looking seaward toward the mouth of the estuary). The *Z*-axis, which corresponds to the *w*

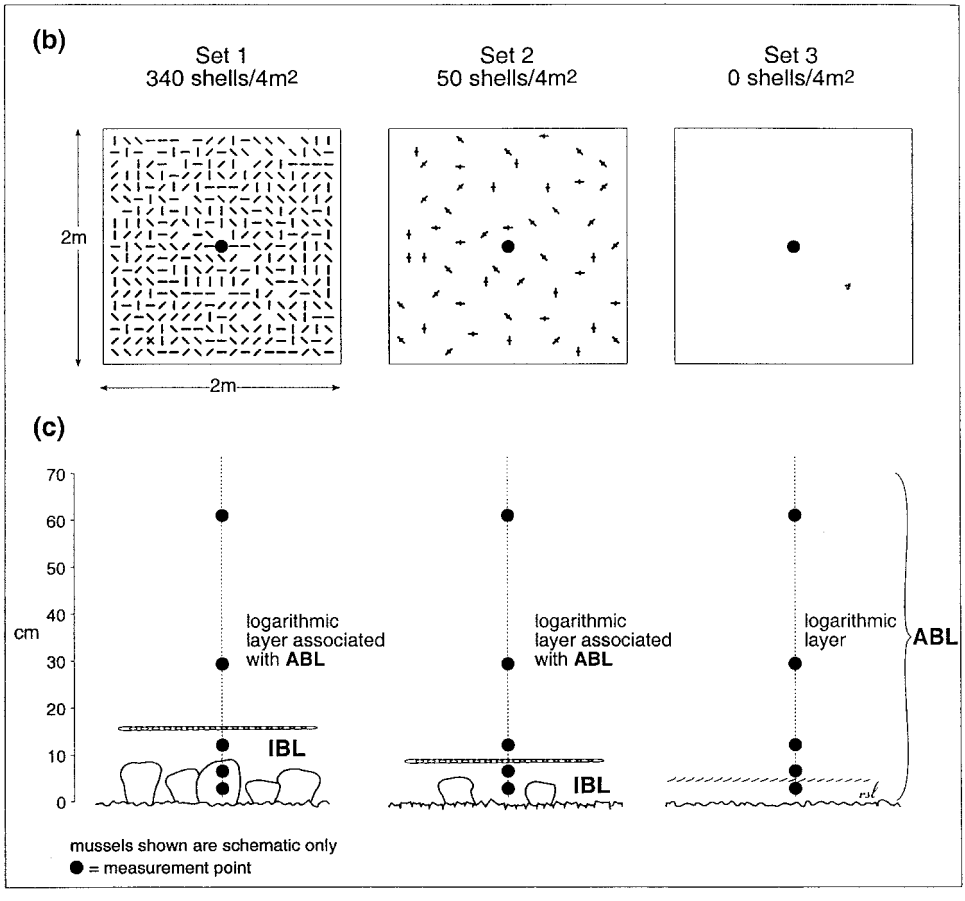

Figure 1. (Continued)

(vertical) velocity component, was oriented in the positive direction toward the water surface. The ADV was fixed to an arm that was cantilevered from a small, rigid, ballasted frame that was designed not to disturb the flow over the plot. The ADV's measuring probe consists of a downward-looking acoustic transmitting sensor mounted on a stem (25 cm long and 7 mm diameter) and surrounded by three equispaced receiving transducers. An important advantage of the ADV over conventional current meters such as propeller current meters and hot-film meters is that it measures water flow in a small sampling volume (0.25 ml), 10 cm away from the sensing elements, without interfering with the flow. The precision of individual velocity samples is in the range 0.25–1.0 cm/s for horizontal velocities u and v and is approximately 30 times smaller than that for the vertical velocity w. Detailed discussion of the ADV performance and measurement errors involved may be found in Nikora and Goring (1998) and Voulgaris and Trowbridge (1998). Noise

contribution to the mean velocities and Reynolds shear stresses (i.e., mean cross-products of velocity components) in our study were low (less than 2–3%).

Measurements were made on a single vertical profile at five logarithmically spaced points in the vertical spanning the 60-cm-thick bottom layer. The ADV sampled at 25 Hz in 4-min bursts every 5 min. During the 1-min off period the height of the sensor was changed by divers attending the instrument and time and nominal instrument elevations were noted. The divers also noted any fish near the sensor and flow disturbances due to wakes from passing boats. In this manner a single vertical profile of velocity measurements was obtained every 25 minutes. A total of 6 profiles was measured over 2.5 hours, first on the flooding tide, and then on the subsequent ebbing tide.

Three sets of measurements were made (Fig. 1b). **Set 1.** Initially, velocity profiles were measured over the patch with *Atrina* at maximum density (340 individuals per 4 m^2). Six profiles on the flooding tide and 6 on the next ebbing tide were obtained, as described above. **Set 2.** After these measurements were completed, *Atrina* were picked back to a density of 50 individuals per 4 m^2 and another 12 velocity profiles were measured (6 flooding and 6 ebbing). Note that 340 and 50 individuals per 4 m^2 represent, approximately, the high and low extremes of the natural range (Green *et al.,* 1998). **Set 3.** Finally, the seabed was picked clean of *Atrina,* smoothed by hand, and the final 12 profiles were obtained. The roughness of the smoothed bed was qualitatively similar to that outside the experimental plot, as was reported by divers and also observed on the underwater pictures.

All measurements were made in the middle of the plot (i.e., 1 m in from the leading edge and 1 m in from the sides). The ADV has a bottom-detection facility and the data generated by this feature were subsequently used to estimate the height of the ADV sampling volume above the sediment bed (with submillimeter/millimeter accuracy). Thus, in our following considerations we use the sediment bed surface as the bed origin. The average elevations above the bed at which measurements were made were 2, 6, 12, 29 and 61 cm, which are depicted in Figure 1c in juxtaposition with the *Atrina* and the various sublayers of the bottom boundary layer, which are described later.

All flow measurements were completed within three days (14–16 November, 1996). During this period there was no ocean swell and very few vessels visited the area. An InterOcean S4 current meter was deployed 1 m above the bed and 20 m from the experimental plot to provide "background conditions" (current speed and direction, water depth, temperature) during experiments.

3. Data analysis

Following convention, in our following considerations we decompose each velocity component into a fluctuating component (denoted by a prime) and an average component (denoted by an overbar, where the average is over the duration of the burst). Thus, $u = \bar{u} + u'$, $v = \bar{v} + v'$ and $w = \bar{w} + w'$, and u, v and w are the orthogonal components of the velocity vector U.

Data were extracted from the initial binary files, checked for unreliable records, and

corrected if necessary. About 4% of the data were rejected as unreliable, principally because of high noise level (Nikora and Goring, 1998; Voulgaris and Trowbridge, 1998). To eliminate potential spikes in the remaining ADV files we used the 'acceleration' criterion. According to this criterion a velocity value u_{n+1} is identified as a spike if both $|u_{n+1} - u_n|/\Delta t > m_1 g$ and $|u'_{n+1}| > m_2 \sigma_u$ are simultaneously valid, where m_1 and m_2 are coefficients, σ_u is the standard deviation of u, g is gravity acceleration and Δt is sampling interval. This criterion assumes that the local acceleration cannot exceed a given acceleration threshold. From numerous tests, it was found that setting $m_1 = 1$ and $m_2 = 1.5$ resulted in the most effective spike identification. The number of spikes identified did not exceed 2.2%, 1.8% and 0.2% of velocity records for u, v and w components, respectively. Spikes were replaced by adjacent previous values, which are assumed to be correct (Otnes and Enochson, 1978). Differences between turbulence parameters calculated from contaminated and cleaned raw data were found to be negligible (in most cases less than 2% difference).

To minimize errors in estimates of turbulence characteristics that are related to sensor misalignment (which causes leakage of the longitudinal velocity component into the other two components), velocity records were further corrected. The following three-step procedure was used which is based on a reasonable assumption that the flow well above *Atrina* (but still far from the water surface) is close to uniform two-dimensional, i.e., the flow satisfies the conditions $\bar{v} = 0$, $\bar{w} = 0$ and $\overline{v'w'} = 0$ (Nikora and Goring, 2000). Firstly, the mean velocity vector was rotated in the X–Y plane to reduce the mean transverse velocity ($\bar{v}$) to zero. Secondly, a similar procedure was applied in the X–Z plane to reduce the mean vertical velocity ($\bar{w}$) to zero. Finally, the data were rotated in the Y–Z plane to reduce the moment $\overline{v'w'}$ (where the overbar denotes a time-average over the duration of the burst) to zero. This three-step procedure was applied for the three upper points in each velocity profile (i.e., above the *Atrina*) and three misalignment angles were obtained for each point. On the assumption that the sensor orientation for all points within the profile was the same and that any differences between points are due to statistical variability, the angles were averaged and used to correct velocity at all points within each profile.

The corrected velocity data were used to calculate the following flow characteristics: mean velocity components; standard deviation for each velocity component; velocity skewness and kurtosis; Reynolds shear and normal stresses; total turbulence energy; relative turbulence intensities; and diagonal (auto-spectra) and non-diagonal (cross-spectra) components of the spectral tensor. These characteristics were calculated using the ADVANS package (Goring *et al.,* 1998). Detailed descriptions and interpretation of turbulence characteristics may be found in Monin and Yaglom (1971; 1975), Hinze (1975) and McComb (1991). Their applications in aquatic ecology were illustrated by Denny (1988), Jumars (1993), Vogel (1994) and Nikora *et al.* (1997), among others.

The main contribution to variability in measured vertical profiles of flow properties is from large-scale flow variability, which in turn is due to large-scale circulation and

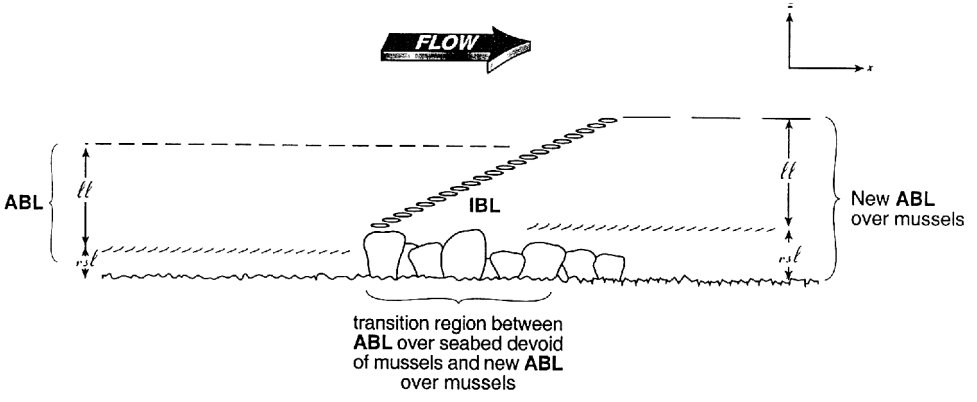

Figure 2. Conceptual picture of boundary-layer structure with flow encountering an *Atrina* patch from the left.

two-dimensional turbulence. An approximate analysis suggests that uncertainty in estimates of flow properties due to large-scale flow variability significantly exceeds instrumental noise and may reach 15–30%. To reduce variability and improve clarity of results, we present profiles averaged by tide phase (i.e., flood and ebb) and profiles averaged by set (i.e., high, low and zero *Atrina* density). The tide-phase-averaged profiles retain variability due to large-scale flow effects and any differences in hydrodynamics on flood and ebb tides, which together may mask effects on the flow of changing bed roughness (i.e., *Atrina* density). The set-averaged profiles most clearly show the effects of changing bed roughness.

4. Conceptual picture of boundary-layer flow over *Atrina* patches

At this point, it is worthwhile establishing a conceptual picture of boundary-layer flow against which the results can be interpreted (Fig. 2). The near-bed part of the fully rough turbulent boundary layer under steady, uniform flow over a level, uniform bed can be divided into two layers: the logarithmic layer (ll) and the roughness sublayer (rsl). Although the instantaneous flow is turbulent—and therefore "three-dimensional"—in the logarithmic layer, the time-averaged motion is "two-dimensional," that is, the mean vertical and mean transverse velocities are both zero. The mean downstream velocity varies systematically with elevation above the bed (to be precise: it varies directly with the logarithm of the height above the bed, hence the name of the layer). The instantaneous flow is also turbulent in the underlying roughness sublayer (slightly above and below the roughness tops), but here things are not made simpler by time-averaging. That is, both the mean transverse and mean vertical velocities are nonzero and, furthermore, there is no obvious systematic variation of any mean velocity component with distance above the bed. The Reynolds stress is essentially constant throughout the logarithmic layer, but it smoothly decreases to zero approaching the bed in the underlying roughness sublayer. This

reduction is due to appearance of new players in the momentum balance within the roughness sublayer, viz., viscous drag on the bed/roughness elements, dispersive stresses, and form drag. As a result, the primary Reynolds stress reduces, to keep the total stress constant. It should be emphasised that these new terms in the momentum balance appear explicitly only in the spatially-averaged momentum equations (Raupach *et al.,* 1991; Nikora *et al.,* 2001). For instance, the dispersive stresses appear as a result of spatial averaging in the same way that turbulent stresses appear in the Reynolds equations as a result of time averaging of the Navier-Stokes equations. In other words, the dispersive stresses are due to spatial disturbances in time-averaged flow. The same applies to the viscous and form drag components.

When the current, with its associated "ambient" boundary layer (ABL) comprising an ll and an rsl, encounters a change of bed roughness—such as the leading edge of a patch of *Atrina*—an "internal" boundary layer (IBL) develops at the base of the ABL. The IBL grows downstream until it completely replaces the ABL, thus becoming the new ABL. The new ABL comprises a new roughness sublayer, which is attached to the new roughness elements (*Atrina* in this example), and a new logarithmic layer, which is associated with the new rsl. The IBL can be thought of as embedded within and entirely independent of the ABL (Antonia and Luxton, 1971). One consequence of that independence is that the Reynolds stress does not change smoothly across the boundary between the ABL and IBL. More details about ABL and IBL structure and dynamics may be found in Townsend (1998).

With the above conceptual picture established, we can give context to the experimental measurements. The set-3 measurements were intended to depict the structure of the ABL over seabed devoid of *Atrina* and, furthermore, the measurements were intended to span the rsl–ll boundary. The set-1 (340 *Atrina* per 4 m^2) and set-2 (50 *Atrina* per 4 m^2) measurements were intended to depict the changes in boundary-layer structure that occur when the tidal current encounters patches at areal densities reflecting the natural range of densities for *Atrina* in this estuary. Since the measurements were made only 1 m downstream of the leading edge of the patch, it is unlikely that the ABL at that point would be completely replaced by the new boundary layer attached to the *Atrina*. Thus, we expect both the set-1 and set-2 measurements to span the IBL and the logarithmic layer associated with the ABL (Fig. 2).

5. Results

a. Background conditions

Measurements were conducted over three tidal cycles that were similar (Fig. 3). Local acceleration was negative when the flood-phase measurements were being made and was positive during ebb-phase measurements. Suspended-sediment concentration, temperature and salinity were not measured and so it was not possible to evaluate effects of density stratification directly. However, it would be reasonable to neglect these effects in our

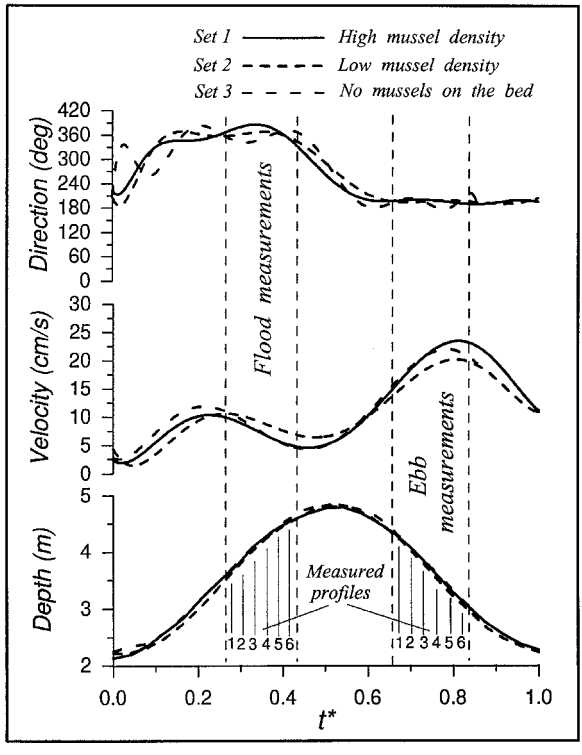

Figure 3. Background conditions at the site measured by the S4 current meter. Data are plotted against normalized time $t^* = (t - t_0)/T$ where t_0 is time between successive minimum water levels and T is tide period.

particular task given the shallow water and energetic tidal flows. Furthermore, stratification of the bottom boundary layer by suspended sediments is unlikely because the water was always either clear or there was a well-mixed washload with no discernible gradient in suspended-sediment concentration. Washload at other times at this same site has been measured at 18–60 ppm, which is less than the value (order 10^2 ppm) that is thought to begin affecting *Atrina* feeding (unpublished data). The global Reynolds number, $\mathrm{Re} = VD/\nu$ (D is the flow depth, V is reference velocity from the InterOcean S4 current meter and ν is kinematic viscosity) was in the range 200,000–750,000. Thus, we expect a reasonably developed turbulence regime at the experimental site.

b. Distribution of mean velocities and turbulent stresses

For all three sets, the tide-phase-averaged longitudinal velocity $\bar{u}$ is greater for the ebb phase (Fig. 4a). The set-averaged velocity $\bar{u}$ close to the bed is smallest for set 1 (high density *Atrina*), intermediate for set 2 (low density) and greatest for set 3 (zero density), but the vertical profiles of $\bar{u}$ converge higher above the bed (Fig. 4b). Some slight deviation of

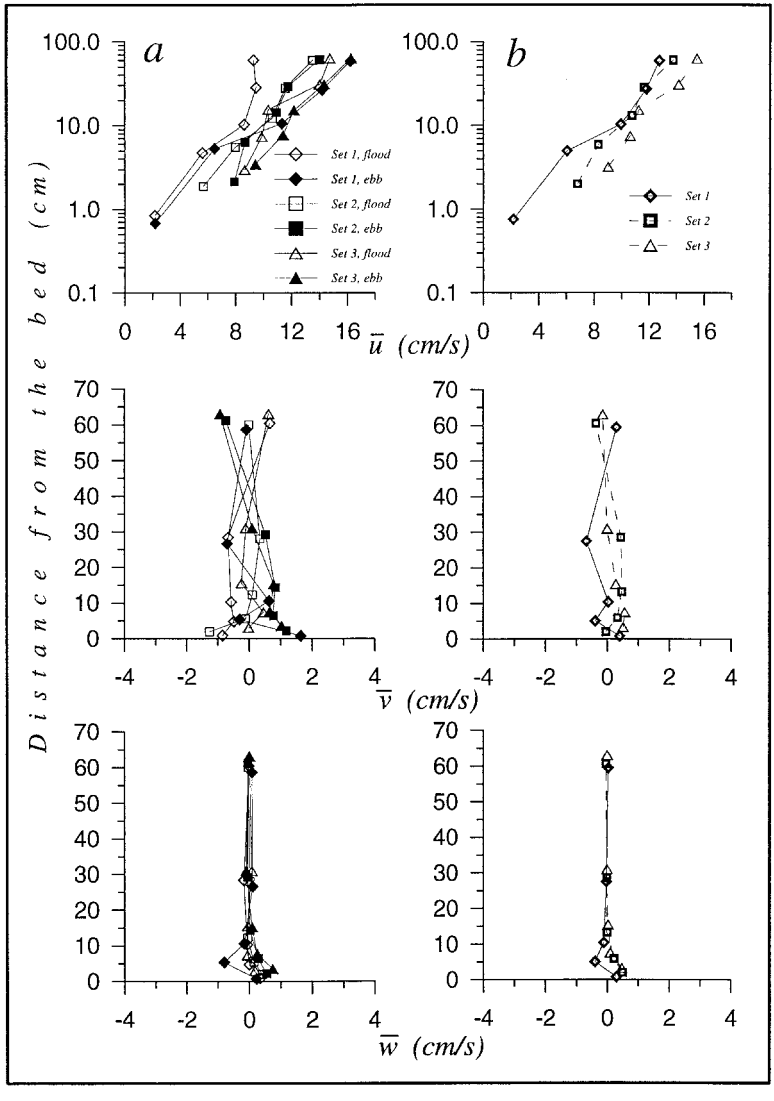

Figure 4. Vertical distributions of mean longitudinal velocity ($\bar{u}$), mean transverse velocity ($\bar{v}$) and mean vertical velocity ($\bar{w}$). (a) Velocity profiles averaged by tide phase (flooding, ebbing). (b) Velocity profiles averaged by tide phase and by experiment set (high, low and zero *Atrina* density).

mean velocities at upper levels for set 3 was most likely due to large-scale flow variability. Mean velocities $\bar{v}$ and $\bar{w}$ are approximately zero high above the bed (Fig. 4b), but closer to the bed there are no consistent patterns in vertical profiles of $\bar{v}$ and $\bar{w}$. There is a noticeable negative peak in both $\bar{v}$ and $\bar{w}$ at the level of the *Atrina* tops for set 1.

Turbulent stresses are represented by the Reynolds tensor $\tau_{ij} = -\rho\overline{u_i' u_j'}$, where ρ is fluid

density and the indices i and j denote velocity component (u is denoted by u_1; v is denoted by u_2; w is denoted by u_3). Because the Reynolds tensor is symmetrical, the turbulent stresses can be fully represented by the six values $-\overline{u'u'}$, $-\overline{v'v'}$, $-\overline{w'w'}$, $-\overline{u'w'}$, $-\overline{u'v'}$ and $-\overline{v'w'}$. The first three are velocity variances, which create normal turbulent stresses, and the last three create turbulent shear stresses.

Figure 5 shows averaged (as in Fig. 4) vertical distributions of Reynolds stresses $-\overline{u'v'}$, $-\overline{u'w'}$ and $-\overline{v'w'}$ for the three sets of measurements. High above the bed, $-\overline{u'v'}$ and $-\overline{v'w'}$ are virtually zero while $-\overline{u'w'}$ is positive and constant, which is expected for two-dimensional flow with constant shear stress. Closer to the bed, the primary Reynolds stress $-\overline{u'w'}$ is not constant with elevation: for sets 2 and 3 (low and zero *Atrina* density, respectively), $-\overline{u'w'}$ decays steadily to approximately zero at the lowest elevation, but for set 1 (high density) there is a large positive peak near the top of the *Atrina* individuals where $-\overline{u'w'}$ is 2–3 times larger than in the layer immediately above. Also, closer to the bed, the stresses $-\overline{u'v'}$ and $-\overline{v'w'}$ are nonzero and comparable to $-\overline{u'w'}$.

Figure 6 shows vertical distributions of the dimensionless correlation coefficient $-\overline{u'w'}/\sigma_u\sigma_w$, where σ_u is the standard deviation of u and σ_w is the standard deviation of w. High above the bed $-\overline{u'w'}/\sigma_u\sigma_w$ is close to 0.3, but closer to the bed $-\overline{u'w'}/\sigma_u\sigma_w$ decays to ~0.1, indicating that the correlation between u and w velocity components is significantly suppressed.

Vertical distributions of total turbulence energy $q = 1/2(\overline{u'u'} + \overline{v'v'} + \overline{w'w'})$ are shown in Figure 7. q is approximately constant higher than 20 cm above the bed and shows no dependence on *Atrina* density. Below 20 cm, q increases toward the bed, and it is larger for sets 1 (high *Atrina* density) and 2 (low density) compared with set 3 (zero density). As was the case with Reynolds stress, there is a large positive peak in the distribution near the level of the *Atrina* tops for the set-1 measurements.

The observation that the primary Reynolds stress $-\overline{u'w'}$ over the bed devoid of *Atrina* (set 3) is constant-with-elevation high in the flow but with a smooth decrease to zero from a lower level confirms that the measurements in that case span a roughness sublayer and logarithmic layer (Fig. 2). Both the $-\overline{u'w'}$ and $\bar{w}$ profiles suggest that the rsl–ll boundary is between ~2 cm (lowest measurement level) and ~6 cm (next highest measurement level). The secondary Reynolds stress $-\overline{v'w'}$ is practically zero at the lowest measurement level, which suggests that the rsl–ll boundary is closer to ~2 cm than it is to ~6 cm. We conclude that, over the bed devoid of *Atrina,* the lowest measurement level is submerged in the roughness sublayer (rsl) formed, most probably, by bed microtopography of biological origin (see Sections 2 and 4), and the upper four measurements were made in the logarithmic layer (ll). Both layers, rsl and ll, are associated with the ABL (Fig. 1c).

The primary Reynolds stress $-\overline{u'w'}$ over the high-density bed (set 1) is also positive and constant-with-elevation high in the flow, but there is not a smooth transition to a region in which $-\overline{u'w'}$ decays continuously to zero at the bed. This suggests that the measurements in that case span a logarithmic layer associated with the ABL upstream of the *Atrina* patch and an embedded IBL (see Fig. 2), which was our expectation. The anomalous $\bar{w}$

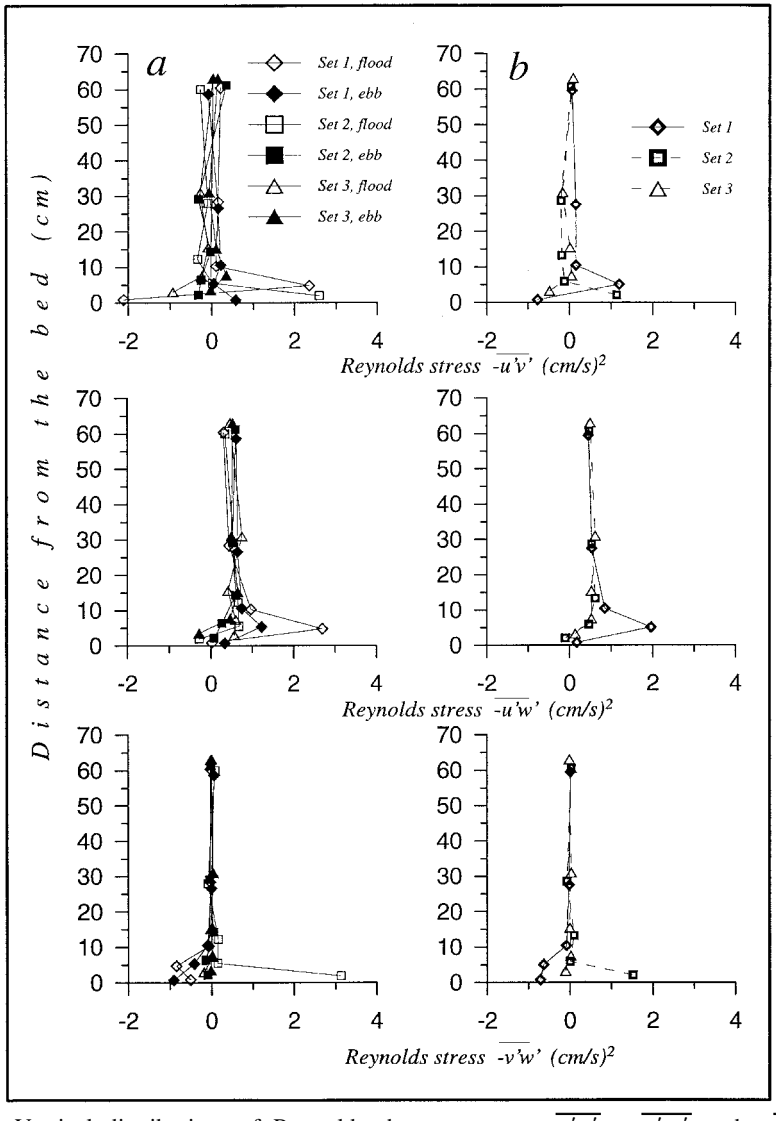

Figure 5. Vertical distributions of Reynolds shear stresses, $-\overline{u'v'}$, $-\overline{u'w'}$ and $-\overline{v'w'}$. (a) Averaged by tide phase (flooding, ebbing). (b) Averaged by tide phase and by experiment set (high, low and zero *Atrina* density).

profile (negative peak near tops of individual *Atrina*) is consistent with this interpretation. Both the $-\overline{u'w'}$ and $\bar{w}$ profiles suggest the IBL–ABL boundary is between ~12 cm (middle measurement level) and ~30 cm (next higher measurement level). Since $-\overline{v'w'}$ is practically zero at the middle level, the boundary is probably closer to ~12 cm. We conclude that, over the high-density bed, the three lowest measurement levels are

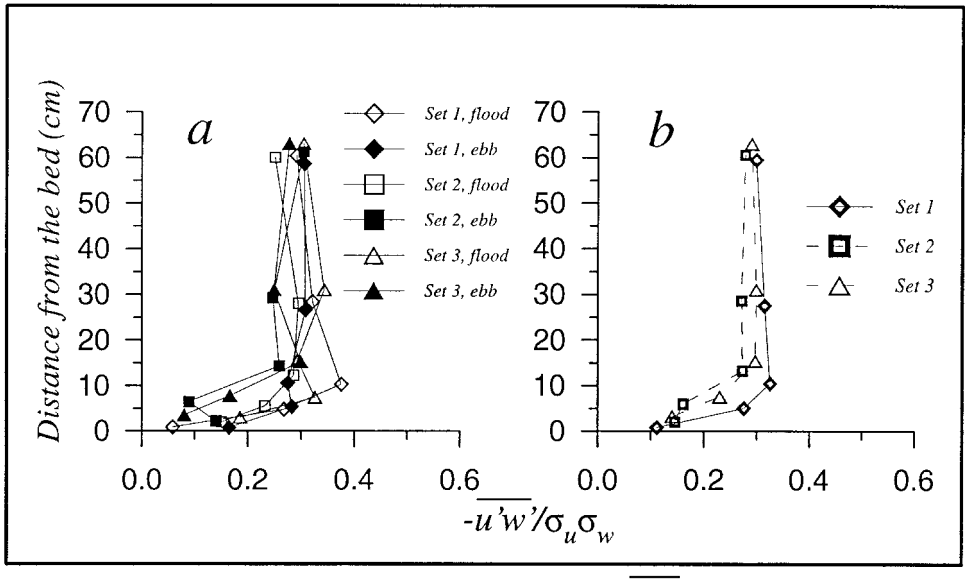

Figure 6. Vertical distributions of the correlation coefficient $-\overline{u'w'}/\sigma_u\sigma_w$. (a) Averaged by tide phase (flooding, ebbing). (b) Averaged by tide phase and by experiment set (high, low and zero *Atrina* density).

submerged in the IBL, and the top two measurements were made in the logarithmic layer associated with the ABL (Fig. 1c).

Because $-\overline{u'w'}$ is positive and constant-with-elevation high in the flow and there is a smooth decrease to zero from a lower level, the set-2 data (low density *Atrina*), like the set-3 data (zero density), imply that measurements span a roughness sublayer that is in equilibrium with an overlying logarithmic layer. This is contrary to our expectation of the existence of an IBL, however, the $-\overline{u'v'}$ profile (Fig. 5b) does suggest the presence of an IBL embedded within but not in equilibrium with an overlying logarithmic layer (Fig. 2). Both the $-\overline{u'v'}$ and $\bar{w}$ profiles suggest that the IBL–ABL boundary is between ~6 cm (second-lowest measurement level) and ~12 cm (next higher measurement level), and since $-\overline{v'w'}$ is practically zero at the second-lowest level, the boundary is probably closer to ~6 cm. We conclude that, for the set-2 (low density) data, the two lowest measurement levels are submerged in the IBL, and the top three measurements were made in the ll associated with the ABL (Fig. 1c).

For convenience, we refer at times in the following to an "external layer" and a "lower layer." For all sets (i.e., all *Atrina* densities), the external layer is the logarithmic layer associated with the ABL. For set 3 (zero *Atrina* density), the lower layer is the rsl associated with the ABL, and for sets 2 (low density) and 1 (high density), the lower layer is the IBL. The analysis of mean velocities and shear stresses suggests that the IBL consisted of a roughness sublayer only as the distance from the patch leading edge was not

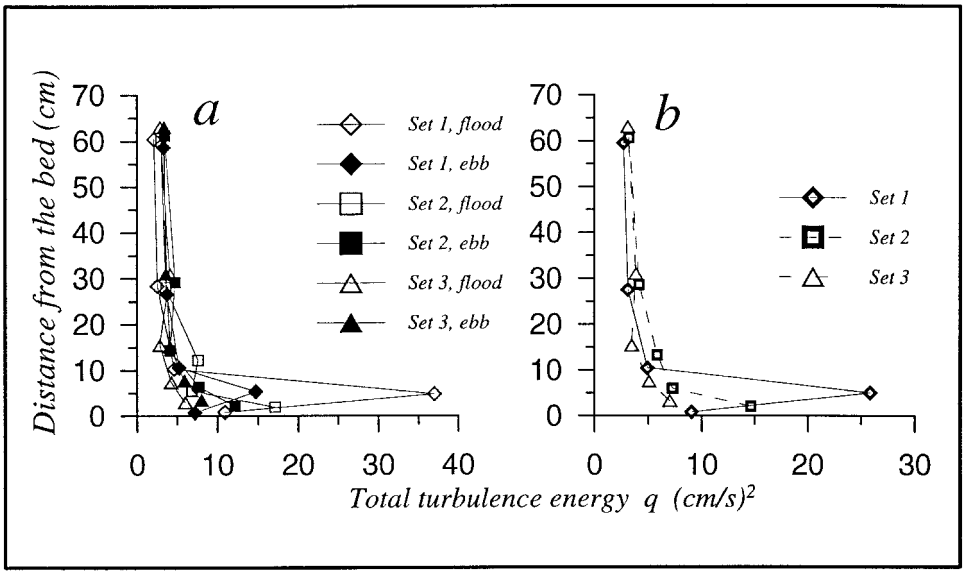

Figure 7. Vertical distributions of the total turbulence energy, q. (a) Averaged by tide phase (flooding, ebbing). (b) Averaged by tide phase and by experiment set (high, low and zero *Atrina* density).

long enough for development of an overlying logarithmic layer associated with the mussel patch. In other words, the IBL thickness was comparable with the exposed mussel height.

c. Friction velocity

For a constant-stress logarithmic layer, the law-of-the-wall applies (e.g., Daily and Harleman, 1966):

$$\bar{u} = \frac{u_*}{\kappa} \ln \frac{z}{z_0} \tag{1}$$

where the friction velocity u_* is the characteristic velocity scale for the layer, $\kappa = 0.41$ is von Karman's constant, z is elevation above the bed and z_0 is hydraulic roughness length. Eq. (2) may be fitted to a measured velocity profile using a least-squares technique to yield estimates of u_* and z_0.

We fitted Eq. (1) to $\bar{u}$ measured at the top two levels for the set-1 (high density *Atrina*) data, at the top three levels for the set-2 (low density) data, and at all levels except the bottom one for the set-3 (zero density) data in order to estimate friction velocity for the logarithmic layer associated with the ABL (Fig. 1c), which we give the symbol u_{*ABL}. Estimates of u_{*ABL} obtained in this way were in the range 0.2–2.5 cm/s and z_{0ABL} was 4×10^{-16}–3.79 cm. These values are likely to be inaccurate because of the limited number of measurement points available for fitting of Eq. (1) and the noisy nature of the $\bar{u}$ profiles

(Fig. 4a). To compensate, we also estimated u_{*ABL} as $u_{*ABL} = ([-\overline{u'w'}]_{avg})^{0.5}$ where $[-\overline{u'w'}]_{avg}$ is the average of $-\overline{u'w'}$ from measurement levels in the logarithmic layer. We consider this second method as providing more accurate estimates of the friction velocity because the $-\overline{u'w'}$ estimates from the logarithmic layer (Fig. 5a) are not as noisy as the $\bar{u}$ profiles.

Figure 8 shows how the mean longitudinal velocity and total turbulence energy scale with friction velocity. For all sets (i.e., all densities of *Atrina*), there is a linear relationship, without hysteresis, between u_{*ABL} and $\bar{u}_{30}$ (Fig. 8a), and between u_{*ABL} and q_{30} (Fig. 8b). Furthermore, the linear relationships in both cases are the same for all sets, which confirms that the properties of the logarithmic layer associated with the ABL are not affected by the *Atrina*. The drag coefficient $C_{30} = (u_{*ABL}/\bar{u}_{30})^2$ is 0.0029 for the logarithmic layer associated with the ABL, which is similar to C_{100} measured by Green *et al.* (1998) in this same estuary over a flat bed devoid of *Atrina*.

We estimated the characteristic velocity scale u_{*IBL} for the IBL over both the set-1 (high density *Atrina*) and set-2 (low density) beds as $u_{*IBL} = ([-\overline{u'w'}]_{max})^{0.5}$ where $[-\overline{u'w'}]_{max}$ is the maximum Reynolds stress below the logarithmic layer (Fig. 5a). u_{*IBL} was 1.4 to 1.8 (set 2) and 1.6 to 2.9 (set 1) times larger than u_{*ABL}.

Scaling of mean velocity and q in the IBL is more complicated than in the ABL. For instance, $u_{*IBL}/\bar{u}_6$ varies with set, which reflects the different bed roughnesses (Fig. 8c). The drag coefficient implied by $u_{*IBL}/\bar{u}_6$ is greatest for set 1 (high density *Atrina*) and least for set 3 (zero density) (Fig. 8c). There is no clear relation between u_{*IBL} and q_6 for both sets 1 and 2 (Fig. 8d), which indicates that the shear stress in the IBL is not in equilibrium with the turbulent energy (Townsend, 1998).

The minimum observed *Atrina* protrusion above the bed (h) of 4 cm and the minimum u_{*IBL} of 0.35 cm/s equate to a minimum roughness Reynolds number ($\mathrm{Re}_* = u_{*IBL}h/\nu$) of 140, which is much larger than the critical value (30–70) for transition to a dynamically rough bed (Monin and Yaglom, 1971). Hence, the *Atrina* patch represented a completely dynamically rough surface at all times.

d. Turbulence intensity

Relative turbulence intensities are presented in Figure 9. Two characteristic velocities are used for normalization: u_{*ABL} and $\bar{u}$. For comparison, some averaged values reported for constant-stress laboratory (water) and atmospheric boundary layers (Monin and Yaglom, 1971; Yaglom, 1993) are shown as vertical dashed lines.

As in most previous graphs, vertical distributions of σ_u/u_{*ABL}, σ_v/u_{*ABL} and σ_w/u_{*ABL} reveal two layers (Fig. 9a): an external layer (i.e., the logarithmic layer associated with the ABL), in which relative turbulence intensities are reasonably constant; and a lower layer (corresponds to the IBL for sets 1 and 2, and to the rsl associated with the ABL for set 3), in which intensities increase with increasing proximity to the bed. Our measured values in the external layer are slightly larger than those reported for laboratory boundary layers, but

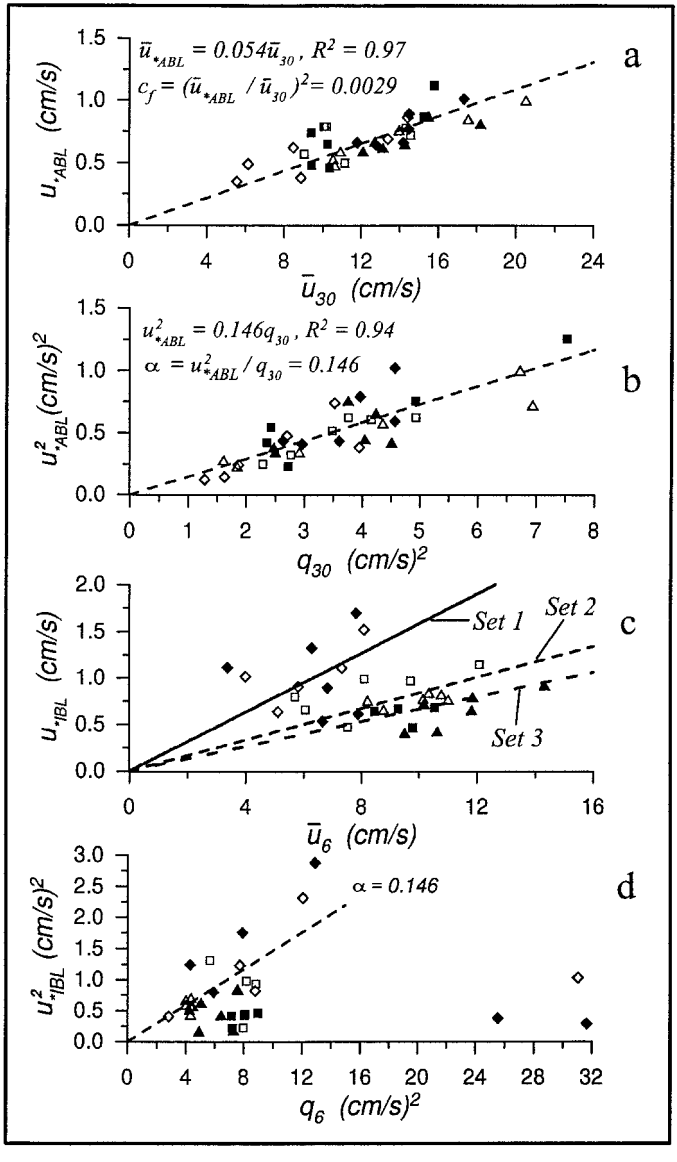

Figure 8. Friction velocity versus mean velocity and total turbulence energy for the ABL (a, b) and for the IBL (c, d). See Figs. 4, 5 or 6 for symbols.

there is better agreement with data reported for atmospheric boundary layers (Yaglom, 1993).

Distributions of turbulence intensities in the form $\sigma_u/\bar{u}$, $\sigma_v/\bar{u}$ and $\sigma_w/\bar{u}$ (Fig. 9b) also demonstrate reasonable collapse of experimental points within narrow regions with

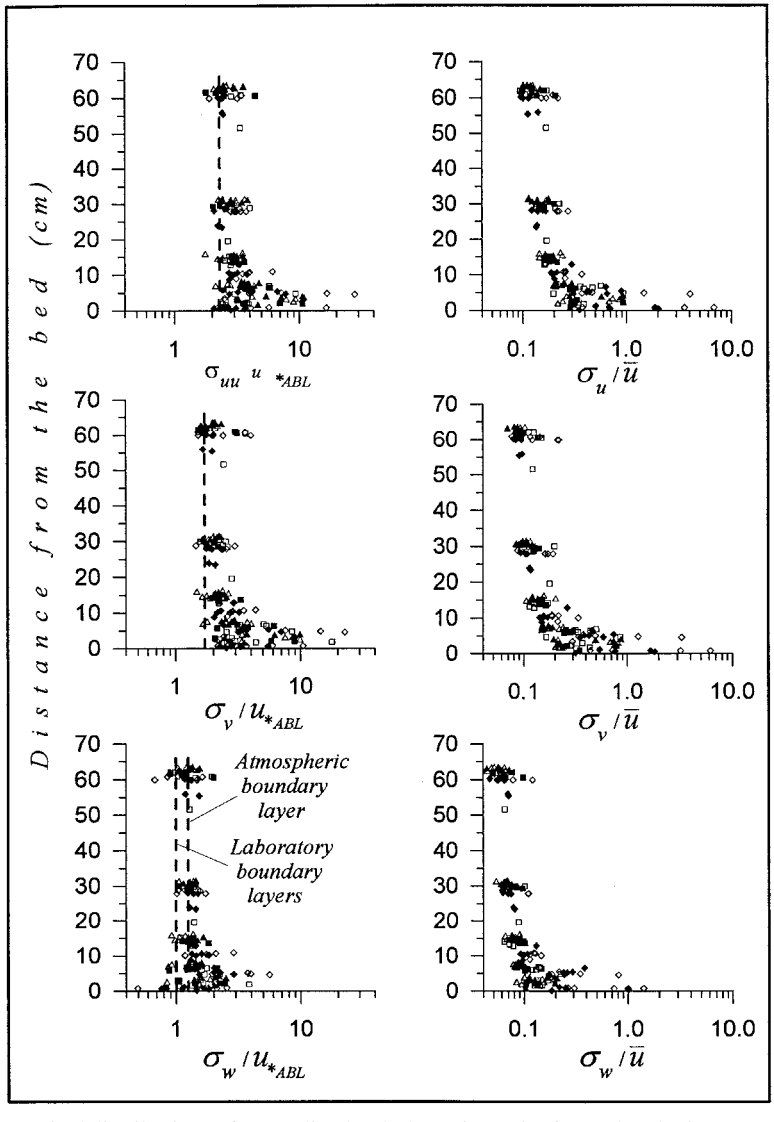

Figure 9. Vertical distributions of normalized turbulence intensity for each velocity component. See Figs. 4, 5 or 6 for symbols.

increased values close to the bed. This increase is especially clear for set 1 (high density *Atrina*). Our measured values of $\sigma_u/\bar{u}$ and $\sigma_w/\bar{u}$ in the external layer agree well with some estimates for tidal flows presented by Heathershaw (1979) (values of $\sigma_v/\bar{u}$ have not been reported yet for tidal boundary layers).

In the external layer, the ratios σ_v/σ_u and σ_w/σ_u, which characterize degree of turbulence anisotropy, are in good agreement with values reported for constant-stress

laboratory and atmospheric boundary layers. However, in the lower layer: (i) σ_v/σ_u tends to 1, reflecting a tendency to isotropy in the horizontal plane; and (ii) σ_w/σ_u decreases, reflecting a tendency to increased anisotropy in the vertical plane, which implies horizontally aligned wake eddies generated behind *Atrina* shells (sets 1 and 2) and behind seabed roughness elements (set 3).

e. Velocity spectra

We have used spectral analysis to describe the structure of velocity fluctuations and spectral energy distribution. The velocity spectral tensor in Cartesian coordinates is $S_{ij}(f)$:

$$S(f) = \begin{vmatrix} S_{uu}, & S_{uv}, & S_{uw} \\ S_{vu}, & S_{vv}, & S_{vw} \\ S_{wu}, & S_{wv}, & S_{ww} \end{vmatrix} \tag{2}$$

where S_{uu}, S_{vv} and S_{ww} are auto-spectra of components u, v and w, respectively, and S_{uv}, S_{uw}, S_{vu}, S_{vw}, S_{wu}, S_{wv} are velocity cross-spectra:

$$S_{ij}(f) = C_{ij}(f) + JQ_{ij}(f) \tag{3}$$

Here f is frequency, $C_{ij}(f)$ and $Q_{ij}(f)$ are co-spectra and quad-spectra (coincident and quadrature parts of the cross-spectrum, $S_{ij}(f)$, respectively), and $J = \sqrt{-1}$ (Panchev, 1971; Bendat and Piersol, 1986). $C_{ij}(f)$ gives useful information about the contribution of motions of various frequencies to the Reynolds stresses since $\overline{u_i'u_j'} = \int_0^\infty C_{ij}(f)df$.

The conceptual and theoretical basis for our spectral analysis derives from Kolmogorov's theory of locally isotropic turbulence (Monin and Yaglom, 1975). More recently, Yaglom (1993) showed that velocity auto-spectra could be divided into four regions from low to high frequency. The first region represents a domain of low-frequency turbulence generation and characterizes the interaction between turbulence and averaged flow. Turbulent eddies forming this region are closely related to external flow scales, which, in our study, is the flow depth. The second region of the auto-spectrum is also a region of relatively large eddies, smaller than the flow depth but larger than distance from the bed. In this region, turbulence production and cascade energy transfer co-exist (Nikora, 1999). The third region (the "inertial subrange") represents high-frequency eddies, assumed to be (quasi) isotropic and smaller than distance from the bed. Isotropic eddies finally break into even smaller "microturbulent" eddies of a much higher frequency, the turbulent energy of which dissipates into heat. The scale of the dissipative eddies is $\eta = (\nu^3/\varepsilon)^{1/4}$, where ν is fluid viscosity and ε is turbulent-energy dissipation rate (Monin and Yaglom, 1975). The physical explanation for this four-range model for wall-bounded turbulent flows is suggested in Nikora (1999).

The most relevant frequency regions for our case study are the second and the third regions. Velocity auto-spectra in the frequency domain can be presented for these regions as (Yaglom, 1993; Nikora, 1999):

$$\left.\begin{aligned} \bar{u}S_{ii}(f)/u_*^2 z &= G_i(fz/\bar{u})^{-1} \\ S_{uu} &\approx 1.9S_{vv} \approx 2.9S_{ww} \end{aligned}\right\} \frac{z}{D} < (fz/\bar{u}) < 1 \tag{4}$$

and

$$\left.\begin{aligned} \bar{u}S_{ii}(f)/u_*^2 z &= D_i(fz/\bar{u})^{-5/3} \\ S_{uu} &= 3/4S_{vv} = 3/4S_{ww} \end{aligned}\right\} 1 < (fz/\bar{u}) \ll \frac{z}{\eta} \tag{5}$$

Eq. (4) refers to the region of intermediate-scale eddies ("minus-1 rolloff") and equation (5) to the inertial subrange ("minus-5/3 rolloff"); G_i and D_i are empirical constants (see Table 2); and i, as before, denotes u, v and w velocity components. Eqs. (4) and (5) are obtained from wave-number spectra using the "frozen turbulence" hypothesis, which can be stated as $S_{ii}(k_w) = \bar{u}S_{ii}(f = k_w\bar{u})$ (Monin and Yaglom, 1975), where $k_w = 1/\lambda$ is wave number and λ is an eddy spatial scale.

Normalized auto-spectra for the external layer (i.e., the logarithmic layer associated with the ABL) are presented in Figure 10a together with plots of equations (4) and (5) evaluated using the empirical constants given in Table 2 (mean values of empirical constants from atmospheric and laboratory boundary layers are used). Eq. (4) describes the observed rate of energy decay (the energy "rolloff") in the intermediate-scale region well, as does equation (5) in the inertial subrange for the w component. For the u and v components, the high-frequency end of the measured spectra turns upward away from the $-5/3$ rolloff predicted by Eq. (5), which can be explained by Doppler noise of the instrument (Nikora and Goring, 1998). Thus, there are no signatures in spectra from the external layer that are related to the *Atrina*. The coefficients G_i and D_i estimated from our dataset are slightly larger than values quoted in the literature for atmospheric and laboratory (water) boundary-layer studies (Table 2). Nevertheless, the ratios of coefficients shown in Eqs. (4) and (5) are confirmed by our dataset.

Spectra from the lower layer (IBL for sets 1 and 2; rsl associated with the ABL for set 3) do not follow scaling relationships (4) and (5), which is not surprising because these layers are characterized by the fact that within them "local conditions" (e.g., proximity to a roughness element) significantly influence turbulence structure. Figure 10b shows velocity spectra near the level of *Atrina* tops averaged over ebb phase of the tide (spectra for floods are similar). There are no appreciable differences between set 2 (low density *Atrina*) and set 3 (zero density). However, spectra from set 1 (high density) are quite different, showing a broad energy input in the range 0.08–0.45 Hz. Two mechanisms could cause this energy input: (1) eddy shedding behind *Atrina* shells (as analysis of turbulence intensities suggests); and (2) *Atrina* activity (water filtering). We can check the former possibility by comparing the frequency range 0.08–0.45 Hz with the characteristic frequency f_{es} for eddy shedding (Scorer, 1978):

$$f_{es} \approx 0.2\,\frac{\bar{u}}{d} \tag{6}$$

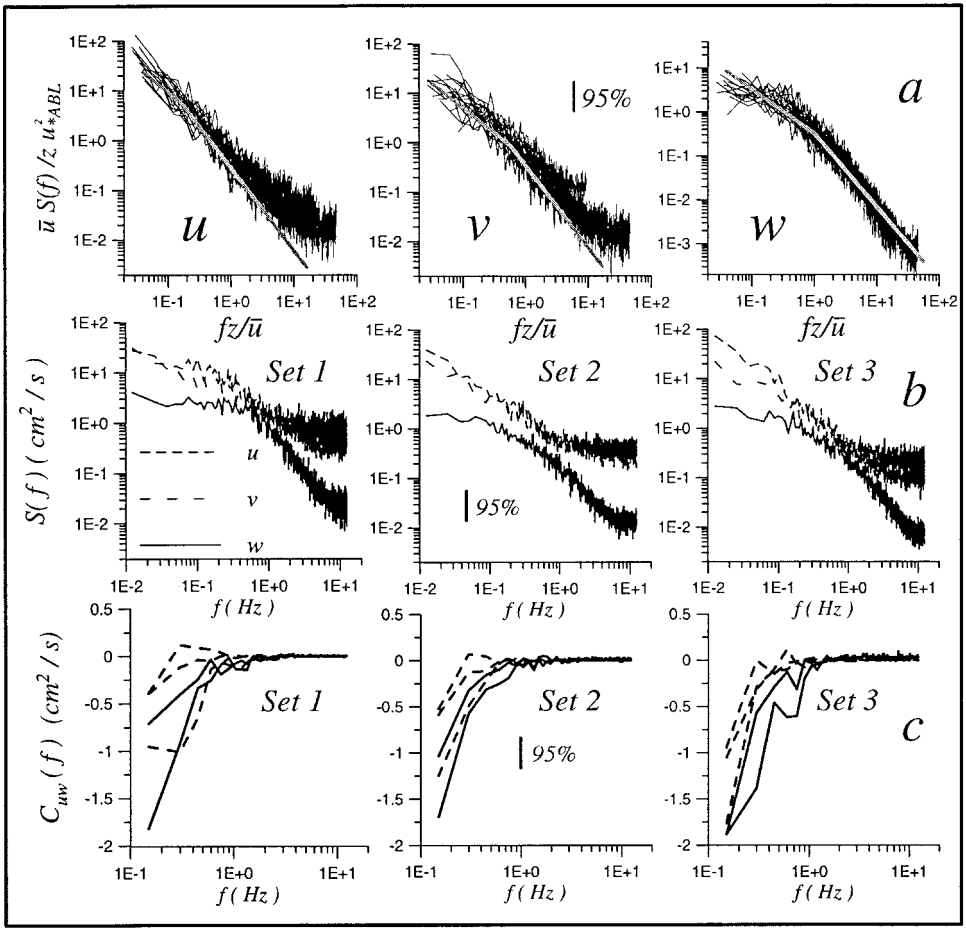

Figure 10. (a) Normalized auto-spectra for the external boundary layer. (b) Auto-spectra at the top of the *Atrina* (averaged over ebb phase of the tide. (c) Co-spectra $C_{uw}(f)$ for profile 5 on the ebb tide (see Fig. 3). Dashed lines denote spectra from the external layer (i.e., logarithmic layer associated with the ABL) and solid lines denote spectra from the lower layer (which is the IBL for sets 1 and 2, and the rsl associated with the ABL for set 3).

where d is the projected shell width. Using 4–11 cm for d in Eq. (7) gives f_{es} in the range 0.08–0.40 Hz, which indicates that eddy shedding from *Atrina* is the likely source of energy input into the spectra. The limitations of our dataset (no measurements of *Atrina* inhalant/exhalant feeding currents were made) prevent us from checking for additional effects of *Atrina* activity on velocity spectra.

From co-spectra $C_{uw}(f)$ we can identify scales of the eddies that contribute most to the primary turbulent stress $-\overline{u'w'}$ (since $\overline{u_i'u_j'} = \int_0^\infty C_{ij}(f)df$). Figure 10c shows typical examples of $C_{uw}(f)$. There are no distinct local peaks in the co-spectra, which might have

Table 2. Average values for empirical constants drawn from atmospheric and laboratory (water) boundary-layer studies (Monin and Yaglom, 1975; Yaglom, 1993), and values derived from the present dataset (measurements over all beds in the logarithmic layer associated with ABL).

	G_u	G_v	G_w	D_u	D_v	D_w
Atmospheric	0.95	—	0.35	0.26–0.28	—	0.32–0.35
Laboratory (water)	0.8–1.1	0.50	0.30	0.26	0.35	0.35
Present study	1.11	0.59	0.37	0.35	0.41	0.37

represented systematic influence of *Atrina* on the flow. Co-spectra ordinates tend to zero as frequency increases and in fact become statistically indistinguishable from zero at some critical frequency. This critical frequency tends to decrease with increasing distance from the bed, changing from 0.8–1.1 s^{-1} in the lower layer to 0.2–0.5 s^{-1} at 60 cm above the bed (Fig. 10c). Using the frozen-turbulence assumption to convert critical frequency to a length scale, we find that the scales of the smallest eddies contributing to $-\overline{u'w'}$ increase from 3–6 cm in the lower layer to 55–65 cm at 60 cm from the bed, which matches expectations, as follows. Firstly, in the IBL attached to the *Atrina,* the size of stress-contributing eddies (3–6 cm) is similar to the width of exposed parts of *Atrina* shells (4–11 cm), which generate turbulence. Secondly, for the logarithmic layer over the rsl attached to the bare bed (set 3) and over the IBL attached to the beds with *Atrina* (sets 1 and 2), the size of stress-contributing eddies correlates with distance from the bed (~60 cm).

It is noteworthy that co-spectra are close or equal to zero over the inertial subrange of frequencies that was identified from the analysis of auto-spectra, which is to be expected from Kolmogorov's theory of local isotropy (Monin and Yaglom, 1975). Energetic motions at low frequencies within the IBL, as seen in both auto- and co-spectra, may be interpreted as a sign that large-scale eddies that were generated in the external layer penetrate the IBL.

6. Discussion

The results illustrate different aspects of the *Atrina* habitat and interactions between *Atrina* and ambient flow at the patch scale (see Table 1).

a. Ambient flow

The "bulk parameters" of the benthic boundary layer (i.e., the reference velocity and the friction velocity) underneath the steady, uniform ambient flow change during the tidal cycle and are therefore time-dependent. Turbulence properties, however, may be considered as time-independent, i.e., they depend on the instantaneous local bulk properties of the flow and not on the flow history.

Measurements made in the absence of *Atrina* revealed a distribution of the primary Reynolds stress that spanned a roughness sublayer and a logarithmic layer that are in equilibrium with each other. We deduced the rsl–ll boundary to be ~2 cm above the bed.

Since the bed at the time was devoid of *Atrina,* the rsl and ll in that case are associated with the ambient boundary layer (ABL).

The properties of the rsl associated with the ABL are: (1) vertical and transverse mean velocities deviate from zero and are comparable with $\bar{u}$; (2) primary Reynolds stress $-\overline{u'w'}$ is suppressed at the expense of form drag on roughness elements (bumps and hollows); (3) secondary stresses $-\overline{u'v'}$ and $-\overline{v'w'}$ are not zero and are comparable with $-\overline{u'w'}$; (4) relative turbulence intensity and turbulence energy increase toward the bed; (5) correlation coefficient $-\overline{u'w'}/\sigma_u\sigma_w$ is suppressed and tends to zero toward the bed; (6) velocity spectra deviate from scaling relationships predicted for the logarithmic, constant-stress layer. Time-averaged flow in this layer is three dimensional.

The properties of the logarithmic layer above are: (1) vertical and transverse mean velocities as well as secondary stresses $-\overline{u'v'}$ and $-\overline{v'w'}$ are negligible; (2) primary stress $-\overline{u'w'}$, correlation coefficient $-\overline{u'w'}/\sigma_u\sigma_w$, turbulence intensities and turbulence energy do not change with changing elevation above the bed; and (3) velocity spectra confirm "-1" scaling at low frequencies and "$-5/3$" scaling at high frequencies. Time-averaged flow in this layer is two dimensional.

The presentation of our data in dimensionless form and comparison with other data show that the logarithmic layer observed in our case study is structurally similar to boundary layers observed in other estuaries, the atmosphere and laboratory tunnels. Although some discrepancies were found for some characteristics, they are probably due to instrument noise, statistical variability, and unsteadiness and non-uniformity of the tidal flow.

b. Effects of Atrina and flow-Atrina interactions

Atrina could modify flow in two ways: (1) passive interactions, in which shells act as roughness elements in the same way as any other bluff body; and (2) active interactions, in which momentum is added/subtracted to/from the flow at various scales by pumping of water whilst suspension feeding. Because no measurements of *Atrina* feeding activity were made, we are unable to comment on the latter mechanism, although the spectral analysis, for one, indicates that at the patch scale the former mechanism is dominant.

With *Atrina* present on the bed, an internal boundary layer embedded at the base of the ambient-flow boundary layer developed. For *Atrina* spread at 340 individuals per 4 m^2 (set 1) and at 1 m downstream of the leading edge of the patch, the top of the IBL was ~12 cm above the bed, which is 1.3–3 times the height of the shells (i.e., 4–9 cm) protruding above the sediment surface. For the less densely populated bed (set 2; 50 individuals per 4 m^2), the top of the IBL was ~6 cm, which is 0.7–1.5 times the protrusion height. Thus, the observed IBL was still in its infancy, i.e., it consisted of a roughness sublayer only as the distance from the leading edge of the patch was not enough for development of a second, overlying logarithmic layer.

We expect the logarithmic layer associated with the ABL to overlie the IBL attached to the *Atrina.* The discontinuity in the vertical distribution of the primary Reynolds stress is evidence that the IBL was not in equilibrium with the overlying external layer. Our

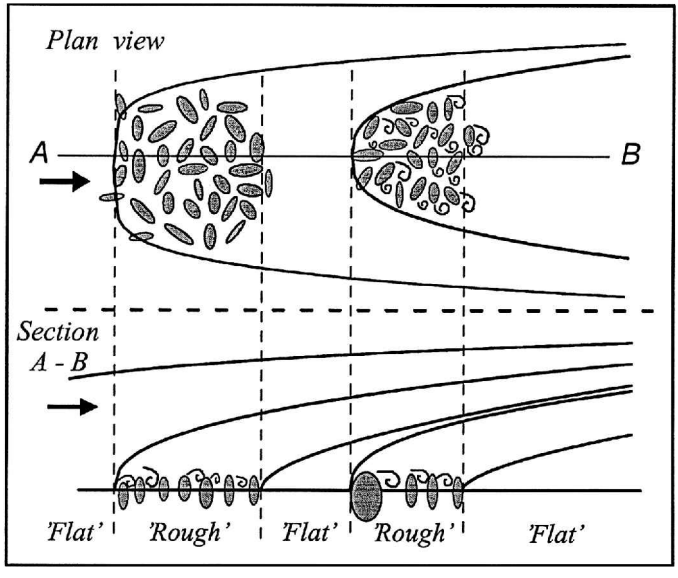

Figure 11. Sketch of flow structure over *Atrina* patch.

analysis also confirms that the properties of the external layer over *Atrina* were identical to the properties of the logarithmic layer over the bed devoid of *Atrina*. Thus, our expectation that the *Atrina* influence on the flow is confined to an IBL that develops within the logarithmic layer of the ABL is confirmed. Furthermore, the properties of the ambient layer—including over the *Atrina* patch—depend on upstream roughness and have no relation to the patch.

The IBL attached to the *Atrina* is structurally similar to the rsl at the base of the ABL in that the flow in both is three dimensional. There are, however, quantitative differences. Compared to the rsl associated with the ABL, the IBL attached to the *Atrina* shows: (1) significantly reduced values of mean longitudinal velocity; (2) increased values of total turbulence energy, turbulent stresses and turbulent intensities; (3) stronger deviation of velocity spectra from the scaling laws for two-dimensional flows; (4) input of energy at low frequencies (0.08–0.45 Hz) in auto-spectra, which can be explained, as a first approximation, by eddy shedding behind shells. Most of the differences between flow in the IBL and flow in the rsl associated with the ABL were more profound over the patch with high *Atrina* density (set 1). Finally, vertical distributions of turbulence characteristics mostly displayed local peaks at the level of shell tops, which agrees well with measurements over other rough beds and with theoretical predictions (Nikora *et al.,* 2001). Figure 11 summarizes the above properties.

c. Ecological implications

Previous ecological studies have indicated the potential for *Atrina* to influence, via flow modifications, benthic community composition at the spatial scales studied in this

experiment (Cummings *et al.,* 1998, 2001). The results presented herein provide some insight into possible mechanisms. The internal boundary layer that envelops the *Atrina* patch is a zone of lower mean longitudinal velocity but more energetic turbulence relative to the ambient boundary layer. Thus, the lower longitudinal velocity translates into shelter, whereas more energetic turbulence translates into increased vertical exchange between the external layer and the IBL. The latter will enhance the flux of nutrients, colonists and suspended sediments and might have implications for deposition and resuspension of organically rich biodeposits. Enhanced turbulent fluxes might account for an observed lack of consistent negative relationships between *Atrina* and other, smaller, suspension feeders found in *Atrina* patches (Cummings *et al.,* 2001). Nevertheless, broader-scale hydrodynamic variations (for example, flow variability at the scale of the estuary) have proved to be useful in developing statistical models to explain relationships between *Atrina* and macrobenthic community structure. This implies that relationships between *Atrina* and macrobenthic community structure at the 10^0–10^2-m scale are not derived solely from within-patch hydrodynamic processes. The scale-dependent nature of the interaction between *Atrina* and flow illustrates how the biological processes that are important can depend on hydrodynamics (Thrush *et al.,* 2001).

d. Implications for modelling phytoplankton consumption and bivalve growth

A number of models describing interactions between flow and suspension feeders have been proposed (Wildish and Kristmanson, 1984, 1997; Frechette *et al.,* 1989; Monismith *et al.,* 1990; O'Riordan *et al.,* 1993, 1995). Among them O'Riordan *et al.*'s (1995) approach is the most comprehensive. However, even this approach is based on heavily simplified, time-averaged, two-dimensional momentum and advection-diffusion equations which ignore the flow heterogeneity and three-dimensionality in the near-bed region above and within the mussel 'canopy.'

Our results suggest that to overcome the problem of spatial heterogeneity in flow properties, the time-averaged momentum and mass-conservation (e.g., advection-diffusion) equations should be spatially averaged and one should operate with smoothed flow variables in both the space and time domains. Spatial averaging over appropriate length scales (Table 1) not only smoothes small-scale perturbations in time-averaged flow properties but also introduces new terms of physical significance (Raupach and Shaw, 1982; Raupach *et al.,* 1991; Kaimal and Finnigan, 1994). For example, the new terms, form drag and dispersive (form-induced) stresses, appear in the spatially averaged momentum equations, and analogous terms, sink/source and dispersive fluxes, also appear in the spatially averaged advection-diffusion equation. Note that the new terms are not *ad hoc;* they arise explicitly as a result of the spatial averaging. This methodology has been developed in atmospheric physics (Kaimal and Finnigan, 1994) and can be successfully extended for the problem of *Atrina*—flow interactions, which are multi-scale phenomena by nature (Fig. 11, Table 1). The spatial averaging approach can help to avoid shortcomings of the previous models, take into account effects of bivalve pumping directly, and,

even more importantly, can create a rigorous basis for resolving scaling problems in benthic ecology (Raffaelli *et al.,* 1994). This view is summarized in Table 1.

7. Conclusions

The field measurements of flow over the *Atrina* patches reveal two distinct layers: an external boundary layer and an embedded internal boundary layer attached to the *Atrina.* The structure of the external boundary layer is conditioned by the roughness upstream of the patch. For the patches observed in this study, the external boundary layer corresponds to the logarithmic layer associated with the upstream roughness (that is, it is the logarithmic layer associated with the ambient flow), and, as such, is essentially two dimensional. In contrast, the internal boundary layer consisted of a roughness sublayer only and, as such, is essentially three dimensional. Compared to the roughness sublayer associated with the ambient flow, mean longitudinal velocities are smaller and turbulence is more energetic in the internal boundary layer attached to the *Atrina.* Furthermore, the differences are greater for the patch with higher density of *Atrina* compared to the lower-density patch. *Atrina* therefore alter the boundary-layer flow in measurable ways. The information on turbulence structure from this study can be used to improve existing models of suspension-feeder–flow interactions.

We suggest that features of the internal boundary layer may be ecologically significant. The IBL that envelops the *Atrina* is a zone of lower mean longitudinal velocities but more energetic turbulence relative to the ambient boundary layer. The former translates into shelter, which some organisms might take advantage of, and the latter translates into increased vertical exchange across the top of the IBL, which might enhance fluxes of nutrients, colonists and suspended sediments, and might have implications for deposition and resuspension of organically rich biodeposits.

In this study, we have analyzed *Atrina*–flow interactions within the leading-edge region (i.e., the region where the internal boundary layer is still growing and "consuming" the ambient boundary layer) of an artificial *Atrina* patch. A new set of experiments over a natural *Atrina* patch in both the leading-edge and 'fully developed' regions could identify the importance of shell orientation, lacunarity, and interactions between the ambient flow and the IBL. Such new measurements should be supplemented with suspended-sediment and phytoplankton measurements, which will provide information on the concentration boundary layer over the *Atrina* bed. To separate effects of active and passive *Atrina*–flow interactions, it would be helpful to make measurements over active animals, and then to repeat the same measurements over neutralized animals.

Acknowledgments. The research was funded by the Foundation for Research Science and Technology (New Zealand) under contracts CO1517 (Ecosystem Dynamics in Estuaries), CO1X0024 and its predecessor CO1618 (Effects of Sediments on Estuarine Ecosystems). We thank Rod Budd and Andy Hill for assistance in the field, Stephanie Brown for preliminary data analysis, and Judi Hewitt for providing data on suspended-sediment concentrations. Instrumentation was purchased through NIWA's strategic capital investment programme, for which we thank Dr Rick Pridmore.

APPENDIX

Notations

C_{30}	drag coefficient at 30 cm above the bed, $C_{30} = (u_{*ABL}/\bar{u}_{30})^2$
C_{100}	drag coefficient at 100 cm above the bed
C_{ij}	co-spectrum of velocity components u_i and u_j
d	shell width
D	depth
D_i	empirical constant pertaining to the ith component of velocity
f	frequency
f_{es}	characteristic frequency of eddy shedding
g	acceleration due to gravity
G_i	empirical constant pertaining to the ith component of velocity
h	height of *Atrina* protrusion above bed
J	$\sqrt{-1}$
k_w	eddy wavenumber
m_1	coefficient in "acceleration criterion"
m_2	coefficient in "acceleration criterion"
N	number of observations
Re	flow Reynolds number
Re_*	roughness Reynolds number, $\mathrm{Re}_* = u_{*IBL}h/\nu$
S_{ii}	auto-spectrum of velocity component u_i
S_{ij}	cross-spectrum of velocity components u_i and u_j
t	time
t_0	time between successive minimum water levels
t^*	normalized time, $t^* = (t - t_0)/T$
T	tide period
q	total turbulence energy
q_6	total turbulence energy at ~6 cm above the bed
q_{30}	total turbulence energy at ~30 cm above the bed
Q_{ij}	quadrature-spectrum of velocity components u_i and u_j
u	component of flow velocity in X direction (up and down channel)
$\bar{u}$	mean (burst-averaged) part of u
u'	fluctuating part of u
u_i	ith component of the flow velocity ($i = 1$ signifies u; $i = 2$ signifies v; $i = 3$ signifies w)
u_*	friction velocity
$\bar{u}_6$	mean longitudinal (down-channel) flow speed at ~6 cm above the bed
$\bar{u}_{30}$	mean longitudinal (down-channel) flow speed at ~30 cm above the bed
u_{*ABL}	friction velocity for the logarithmic layer associated with the ABL
u_{*IBL}	friction velocity for the internal boundary layer

$\overline{u_i' u_j'}$	velocity moment formed from the fluctuating parts of the ith and jth components of the flow velocity. For $i = j$, $\overline{u_i' u_j'}$ is a velocity variance or normal turbulent stress. For $i \neq j$, $\overline{u_i' u_j'}$ is a turbulent (Reynolds) shear stress.
$[-\overline{u'w'}]_{\text{avg}}$	average moment for the layer
$[-\overline{u'w'}]_{\max}$	maximum moment in the layer
U	flow velocity vector
v	component of flow velocity in Y direction (across channel)
$\bar{v}$	mean (burst-averaged) part of v
v'	fluctuating part of v
V	reference velocity
w	component of flow velocity in Z direction (vertical)
$\bar{w}$	mean (burst-averaged) part of w
w'	fluctuating part of w
X	horizontal direction parallel to main channel
Y	horizontal direction across main channel
Z	vertical direction
z	elevation above the bed
z_0	hydraulic roughness length
z_{0ABL}	hydraulic roughness length for the logarithmic layer associated with the ABL
Δt	sampling interval
ϵ	turbulent-energy dissipation rate
η	dissipation scale
κ	von Karman's constant
λ	eddy length
ν	kinematic fluid viscosity
ρ	fluid density
σ_{u_i}	standard deviation of the ith component of velocity
τ_{ij}	Reynolds tensor, $\tau_{ij} = -\rho\overline{u_i' u_j'}$

Abbreviations

ABL	ambient boundary layer
IBL	internal boundary layer
ll	logarithmic layer
rsl	roughness sublayer

REFERENCES

Antonia, R. A. and R. E. Luxton. 1971. The response of a turbulent boundary layer to a step change in surface roughness. Part 1. Smooth to rough. J. Fluid Mech., *48,* 721–761.

Bendat, J. S. and A. G. Piersol. 1986. Random Data. Analysis and Measurements Procedures, John Wiley and Sons, NY, 566 pp.

Butman, C. A., M. Frechette, W. R. Geyer and V. R. Starczak. 1994. Flume experiments on food

supply to the blue mussel *Mytilus edulis* L. as a function of boundary layer flow. Limnol. Oceanogr., *39,* 1755–1768.

Cole, B. E., J. K. Thompson and J. E. Cloern. 1992. Measurement of filtration rates by infaunal bivalves in a recirculating flume. Mar. Biol., *113,* 219–225.

Cummings, V. J., S. F. Thrush, J. E. Hewitt and G. A. Funnell. 2001. The variable effect of a large suspension-feeding bivalve on infauna: experimenting in a complex system. Mar. Ecol. Prog. Ser., *209,* 159–175.

Cummings, V. J., S. F. Thrush, J. E. Hewitt and S. J. Turner. 1998. The influence of the pinnid bivalve *Atrina zelandica* (Gray) on benthic macroinvertebrate communities in soft-sediment habitats. J. Exp. Mar. Biol. Ecol., *228,* 227–240.

Daily, J. W. and D. R. F. Harleman. 1966. Fluid Dynamics, Addison-Wesley, Reading, MA, 454 pp.

Denny, M. W. 1988. Biology and the Mechanics of the Wave-Swept Environment, Princeton University Press, Princeton, NJ, 329 pp.

Ertman, S. C. and P. A. Jumars. 1988. Effects of bivalve siphonal currents on the settlement of inert particles and larvae. J. Mar. Res., *46,* 797–813.

Frechette, M., C. A. Butman and W. R. Geyer. 1989. The importance of boundary-layer flows in supplying phytoplankton to the benthic suspension feeder, *Mytilus edulis* L. Limnol. Oceanogr., *34,* 19–36.

Goring, D., V. I. Nikora and S. L. R. Brown. 1998. ADVANS: A suite for turbulence analysis of ADV data. Manual. Part 1. NIWA Internal Report No 11, 55 pp.

Green, M. O., J. E. Hewitt and S. F. Thrush. 1998. Seabed drag coefficient over natural beds of horse mussels (*Atrina zelandica*). J. Mar. Res., *56,* 613–637.

Heathershaw, A. D. 1979. The turbulent structure of the bottom boundary layer in a tidal current. Geophys. J. Roy. Astr. Soc., *58,* 395–430.

Hinze, J. O. 1975. Turbulence, McGraw-Hill, NY, 790 pp.

Jorgensen, C. B. 1996. Bivalve filter feeding revisited. Mar. Ecol. Prog. Ser., *142,* 287–302.

Jumars, P. A. 1993. Concepts in Biological Oceanography. An Interdisciplinary Primer, Oxford University Press, 348 pp.

Kaimal, J. C. and J. J. Finnigan. 1994. Atmospheric Boundary Layer Flows, Oxford University Press, Oxford, 289 pp.

Kraus, N. C., A. Lohrmann and R. Cabrera. 1994. New acoustic meter for measuring 3D laboratory flows. J. Hydraulic Eng., ASCE, *120,* 406–412.

McComb, W. D. 1991. The Physics of Fluid Turbulence, Oxford University Press, Oxford, 572 pp.

Monin, A. S. and A. M. Yaglom. 1971. Statistical Fluid Mechanics: Mechanics of Turbulence, Vol. 1, MIT Press, Boston, MA, 769 pp.

—— 1975. Statistical Fluid Mechanics: Mechanics of Turbulence, Vol. 2, MIT Press, Boston, MA, 874 pp.

Monismith, S. G., J. R. Koseff, J. K. Thompson, C. A. O'Riordan and H. M. Neph. 1990. A study of model bivalve siphonal currents. Limnol. Oceanogr., *35,* 680–696.

Nikora, V. I. 1999. Origin of the "−1" spectral law in wall-bounded turbulence. Phys. Rev. Lett., *83,* 734–737.

Nikora, V. I. and D. G. Goring. 1998. ADV turbulence measurements: can we improve their interpretation? J. Hydraulic Eng., ASCE, *124,* 630–634.

—— 2000. Flow turbulence over fixed and weakly mobile gravel beds. J. Hydraulic Eng., ASCE, *126,* 679–690.

Nikora, V. I., D. G. Goring and B. J. F. Biggs. 1997. On stream periphyton-turbulence interactions. NZ J. Mar. Freshwater Res., *31,* 435–448.

Nikora, V. I., D. G. Goring, I. McEwan and G. Griffiths. 2001. Spatially-averaged open-channel flow over a rough bed. J. Hydraulic Eng., ASCE, *127,* 123–133.

O'Riordan, C. A., S. G. Monismith and J. R. Koseff. 1993. A study of concentration boundary-layer formation over a bed of model bivalves. Limnol. Oceanogr., *38,* 1712–1729.

—— 1995. The effect of bivalve excurrent jet dynamics on mass transfer in a benthic boundary layer. Limnol. Oceanogr., *40,* 330–344.

Otnes, R. K. and L. Enochson. 1978. Applied Time Series Analysis, Vol. 1, Wiley, Chichester, 449 pp.

Panchev, S. 1971. Random Functions and Turbulence, Pergamon Press, NY, 444 pp.

Raffaelli, D. G., A. G. Hildrew and P. S. Giller. 1994. Scale, pattern and process in aquatic systems: concluding remarks, *in* Aquatic Ecology: Scale, Pattern and Process, P. S. Giller, A. G. Hildrew and D. G. Raffaelli, eds., Blackwell Scientific Publications, 601–606.

Raupach, M. R., R. A. Antonia and S. Rajagopalan. 1991. Rough-wall turbulent boundary layers. Appl. Mech. Rev., *44,* 1–25.

Raupach, M. R. and R. H. Shaw. 1982. Averaging procedures for flow within vegetation canopies. Boundary-Layer Meteor., *22,* 79–90.

Scorer, R. S. 1978. Environmental Aerodynamics, Ellis Horwood Lim., NY, 488 pp.

Townsend, A. A. 1998. The structure of turbulent shear flows. Cambridge University Press, Cambridge, 429 pp.

Thrush, S. F., V. J. Cummings, J. E. Hewitt, G. F. Funnell and M. O. Green. 2001. The role of suspension feeding bivalves in influencing macrofauna: variations in response, *in* Organism-Sediment Interactions, J. Aller, R. Aller and S. A. Woodin, eds., University of South Carolina Press, Columbia, SC, (in press).

Vogel, S. 1994. Life in Moving Fluids. The Physical Biology of Flow, 2nd ed, Princeton University Press, Princeton, NJ, 467 pp.

Voulgaris, G. and J. H. Trowbridge. 1998. Evaluation of acoustic Doppler velocimeter (ADV) for turbulence measurements. J. Atmos. Oceanic Tech., *15,* 272–289.

Warwick, R. M., A. J. McEvoy and S. F. Thrush. 1997. The influence of *Atrina zelandica* Gray on nematode diversity and community structure. J. Exp. Mar. Biol. Ecol., *214,* 231–247.

Wildish, D. J. and D. D. Kristmanson. 1984. Importance to mussels of the benthic boundary layer. Can. J. Fish. Aquat. Sci., *41,* 1618–1625.

—— 1997. Benthic Suspension Feeders and Flow. Cambridge University Press, Cambridge, 409 pp.

Yaglom, A. 1993. Similarity laws for wall turbulent flows: their limitations and generalizations, *in* New Approaches and Concepts in Turbulence, Th. Dracos and A. Tsinober, eds., Birkhauser Verlag, 7–27.

Received: *4 October, 1999;* revised: *23 October, 2001.*